

# UC Berkeley

## UC Berkeley Previously Published Works

### Title

On the correlation between material structure and seismic attenuation anisotropy in porous media

### Permalink

<https://escholarship.org/uc/item/4417b56s>

### Journal

Journal of Geophysical Research: Solid Earth, 119(4)

### ISSN

21699313

### Authors

Masson, Y. J  
Pride, S. R

### Publication Date

2014-04-01

### DOI

10.1002/2013JB010798

Peer reviewed

## RESEARCH ARTICLE

10.1002/2013JB010798

## Key Points:

- Anisotropy of seismic attenuation correlates to anisotropy of the heterogeneity
- Ratios of peak attenuation in different directions depend on correlation lengths
- Attenuation anisotropy is demonstrated numerically and modeled analytically

## Correspondence to:

S. R. Pride,  
SRPride@lbl.gov

## Citation:

Masson, Y. J., and S. R. Pride (2014), On the correlation between material structure and seismic attenuation anisotropy in porous media, *J. Geophys. Res. Solid Earth*, 119, 2848–2870, doi:10.1002/2013JB010798.

Received 25 OCT 2013

Accepted 13 MAR 2014

Accepted article online 20 MAR 2014

Published online 17 APR 2014

## On the correlation between material structure and seismic attenuation anisotropy in porous media

Y. J. Masson<sup>1</sup> and S. R. Pride<sup>2</sup>

<sup>1</sup>Institut de Physique du Globe de Paris, Paris, France, <sup>2</sup>Earth Sciences Division, Lawrence Berkeley National Laboratory, Berkeley, California, USA

**Abstract** Through numerical experiments and analytical analysis, we show that a strong correlation exists between anisotropy in the material structure (i.e., the elongation of inclusions present within rocks in the different directions of space) and anisotropy in seismic attenuation (i.e., the values of the inverse quality factors associated with the anisotropic moduli that control wave propagation). This is especially true for weakly anisotropic materials where a power law is shown to relate the aspect ratios of the inclusions (i.e., the ratios of the lengths of the inclusions in the different spatial directions) to the peak attenuation ratios (i.e., the ratios of the maximum values of the quality factors describing wave attenuation in the different spatial directions). Analytical results show that small deviations from this simple power law relation are to be expected for general anisotropic materials. For axisymmetric spheroidal inclusions, a perfectly bijective analytical relation is obtained between aspect ratios of the inclusions and attenuation ratios. This relation is not a power law in general but may be considered to reduce to one as aspect ratios approach 1 (a perfect sphere).

### 1. Introduction

The aim of this paper is to establish a relation between anisotropy in seismic attenuation and the structure of porous materials over mesoscopic scales defined here as those larger than grain sizes but smaller than wavelengths. The mechanism of seismic attenuation treated here is that involving wave-induced fluid flow in porous composites (i.e., rocks). As a wave stresses a material with patches of mesoscale heterogeneity, the various patches each respond with a different fluid pressure which results in mesoscale flow of the viscous fluid and associated loss.

Typical heterogeneities encountered in natural rocks include fractures, stratification, and, in the case of partial saturation, immiscible fluid patches. Many analytical models exist for modeling the induced fluid flow and associated dispersion and attenuation for the various types of heterogeneity. For example, *Pride and Berryman* [2003a, 2003b] and *Pride et al.* [2004] model lithological heterogeneities; *White* [1975], *Knight et al.* [1998], *Johnson* [2001], and *Pride et al.* [2004] model immiscible fluid patches; *White et al.* [1975], *Norris* [1993], and *Gurevich and Lopatnikov* [1995] model layered media; and *Mavko and Nur* [1979], *Dvorkin et al.* [1995], and *Pride et al.* [2004] model grain-scale cracks. Only for the case of macroscopic aligned fractures in porous materials have the effects of seismically induced fluid flow been incorporated into anisotropic attenuation models [e.g., *Chapman*, 2003; *Maultzsch et al.*, 2003; *Chichinina et al.*, 2009; *Baird et al.*, 2013]. Our goal in this paper is to explore and understand how attenuation anisotropy is related to the orientation and anisotropy of mesoscale heterogeneity in the porous material properties.

In what follows, we treat the problem of anisotropic attenuation in poroelastic materials both numerically and analytically. *Masson and Pride* [2007] introduce a computationally efficient method to determine attenuation and dispersion in porous materials that contain an arbitrary amount of mesoscopic-scale heterogeneity. After a brief overview of anisotropy in poroelastic media in section 2, we present our numerical approach for calculating the attenuation associated with the different elastic moduli of an anisotropic porous material in section 3. In section 4, numerical results are given for the dispersion and attenuation associated with porous materials that are locally isotropic but macroscopically anisotropic due to the mesoscale structure. In section 5, an approximate analytical model for the relative attenuations associated with the different elastic moduli is obtained and our main result for the ratio of peak attenuation for different deformation modes presented.

## 2. Anisotropic Poroelasticity

For the general case of a fully anisotropic poroelastic material, the stress-strain relations can be written [e.g., Biot, 1955]

$$\sigma_{ij} = C_{ijkl}\epsilon_{kl} - \gamma_{ij}\zeta, \quad (1)$$

$$-p = \gamma_{ij}\epsilon_{ij} - M\zeta, \quad (2)$$

where  $\sigma_{ij}$  is the overall stress tensor acting on each sample of the porous material,  $\epsilon_{ij}$  is the overall strain tensor,  $p$  is the spatially averaged fluid pressure in the pores, and  $\zeta$  is the so-called “increment in fluid content” (the net volume of fluid entering a sample of porous material divided by sample volume). The elastic moduli are the “undrained” stiffnesses  $C_{ijkl}$  (defined under conditions where  $\zeta = 0$ ), the coupling moduli  $\gamma_{ij}$ , and the fluid-storage coefficient  $M$ . *Berryman and Nakagawa* [2010] discuss many aspects of the nature of the anisotropic poroelastic moduli for orthotropic symmetries.

In the numerical experiments of this paper, we focus on determining the undrained moduli  $C_{ijkl}$  since they are the moduli normally of interest across the seismic band of frequencies. As demonstrated by *Pride* [2005], for circular frequencies  $\omega$  satisfying  $\omega \rho_f k / \eta \ll 1$ , where  $\rho_f$  is fluid density,  $\eta$  is fluid viscosity, and  $k$  is the largest principal value of the permeability tensor, no significant volume of fluid enters or leaves each sample being stressed by a seismic wave, and the material acts as if it is undrained (as if each sample of porous material is effectively sealed from its surroundings so that  $\zeta \approx 0$ ). For water in the pores and for rock permeabilities less than 10 Darcy, this condition is satisfied for all frequencies less than  $10^4$  Hz. Although fluid may not be entering or leaving a sample on average in an undrained seismic-band response, there can be fluid redistributions within a sample (mesoscale flow) that result in the undrained moduli  $C_{ijkl}$  being complex and frequency dependent in the frequency domain.

In general, all of the poroelastic constants  $C_{ijkl}$ ,  $\gamma_{ij}$ , and  $M$  depend on the bulk modulus  $K_f$  of the fluid in the pores. In the limit of very low frequencies ( $\omega \rightarrow 0$ ), where the pressure throughout the pores of each sample is uniform, and under conditions where the framework of grains is made of a single isotropic mineral having bulk modulus  $K_s$ , *Gassmann* [1951] derived how the undrained stiffnesses  $C_{ijkl}$  are related to the drained stiffnesses  $C_{Dijkl}$ , the fluid and solid bulk moduli  $K_f$  and  $K_s$ , and the porosity. That relation is given and used in section 3 in the development of the analytical model.

## 3. Numerical Method

We thus focus on undrained experiments ( $\zeta = 0$ ) with Hooke’s law given by

$$\sigma_{ij} = C_{ijkl}\epsilon_{kl}. \quad (3)$$

Due to the symmetry of the stress, strain, and stiffness tensors, only 21 elastic constants are independent in the most general triclinic case. For simplicity, we limit our study to the case of orthotropic materials, i.e., to materials for which the elastic properties differ in only the orthogonal directions of space. For orthotropic materials, equation (3) can be written in the matrix form

$$\begin{bmatrix} \sigma_{xx} \\ \sigma_{yy} \\ \sigma_{zz} \\ \sigma_{yz} \\ \sigma_{zx} \\ \sigma_{xy} \end{bmatrix} = \begin{bmatrix} M_{11} & M_{12} & M_{13} & & & \\ M_{21} & M_{22} & M_{23} & & & \\ M_{31} & M_{32} & M_{33} & & & \\ & & & G_1 & & \\ & & & & G_2 & \\ & & & & & G_3 \end{bmatrix} \begin{bmatrix} \epsilon_{xx} \\ \epsilon_{yy} \\ \epsilon_{zz} \\ \epsilon_{yz} \\ \epsilon_{zx} \\ \epsilon_{xy} \end{bmatrix} \quad (4)$$

with  $M_{ii} = C_{iiii}$ ,  $M_{ij} = C_{ijij}$ , and  $G_i = 2C_{jkjk}$  (no sum on  $i, j$ , and  $k$ , and  $i \neq j \neq k$ ). There are only nine elastic constants that are independent in an orthotropic material because  $M_{ij} = M_{ji}$ . Note that we have elected here to put the factor of 2 on the shear moduli  $G_i$  instead of on the shear strains  $\epsilon_{ij}$  with  $i \neq j$ .

To numerically determine the undrained elastic moduli  $M_{ij}$  and  $G_i$  of a sample of orthotropic poroelastic material, our approach is to use the finite-difference modeling code and protocol developed by *Masson and Pride* [2007] in which the Biot equations of poroelasticity are solved locally throughout a sample being subjected to either stress or displacement (strain) boundary conditions. The *Masson and Pride* [2007] code

assumes that within the sample being modeled, the poroelastic material is locally isotropic. An overall anisotropic sample is created by having mesoscopic-scale heterogeneity in how the isotropic poroelastic moduli are distributed throughout the sample.

For a rectangular cuboid sample with faces perpendicular to the  $x$ ,  $y$ , and  $z$  directions of space, the moduli  $M_{11}$ ,  $M_{21}$ , and  $M_{31}$  can be computed by applying a time-varying strain  $\epsilon_{xx}(t)$  (or displacement after multiplying the imposed strain by the sample dimension) on the faces perpendicular to the  $x$  axis while imposing zero strain in the direction perpendicular to the other faces (i.e.,  $\epsilon_{yy}(t) = 0$  on the faces perpendicular to the  $y$  axis, and  $\epsilon_{zz}(t) = 0$  on the faces perpendicular to the  $z$  axis). In the numerical simulations, the stress fields are zero outside the cuboid sample and a sealed boundary condition is applied to all faces of the sample (i.e., no fluid is allowed to enter or escape the sample). The moduli so determined are thus undrained as desired.

The numerical experiments are performed in the time domain and the volume-averaged stress and strain fields  $\langle \epsilon_{xx} \rangle_{\Omega}(t)$ ,  $\langle \sigma_{xx} \rangle_{\Omega}(t)$ ,  $\langle \sigma_{yy} \rangle_{\Omega}(t)$ , and  $\langle \sigma_{zz} \rangle_{\Omega}(t)$  are recorded versus time. Here  $\langle x \rangle_{\Omega}$  denotes the spatial average of the field  $x$  over the region  $\Omega$  occupied by the sample. Finally, once the numerical experiment is finished, the moduli  $M_{11}$ ,  $M_{21}$ , and  $M_{31}$  can be computed as a function of frequency by taking a Fourier transform (FT) of the volume-averaged fields recorded as a function of time and by computing the ratios

$$M_{11}(\omega) = \frac{\text{FT} \{ \langle \sigma_{xx} \rangle_{\Omega}(t) \}}{\text{FT} \{ \langle \epsilon_{xx} \rangle_{\Omega}(t) \}} \quad (5)$$

$$M_{21}(\omega) = \frac{\text{FT} \{ \langle \sigma_{yy} \rangle_{\Omega}(t) \}}{\text{FT} \{ \langle \epsilon_{xx} \rangle_{\Omega}(t) \}} \quad (6)$$

$$M_{31}(\omega) = \frac{\text{FT} \{ \langle \sigma_{zz} \rangle_{\Omega}(t) \}}{\text{FT} \{ \langle \epsilon_{xx} \rangle_{\Omega}(t) \}}. \quad (7)$$

The moduli so obtained are complex in general with the negative imaginary parts controlling the amount of energy dissipated by the movement of viscous fluid within the sample (see Appendix A).

The moduli  $M_{12}$ ,  $M_{22}$ , and  $M_{32}$  can be obtained using the same procedure in a second experiment where a time-varying strain  $\epsilon_{yy}(t)$  is applied on the faces perpendicular to the  $y$  axis with zero strain applied to the other faces. In this case, we have

$$M_{12}(\omega) = \frac{\text{FT} \{ \langle \sigma_{xx} \rangle_{\Omega}(t) \}}{\text{FT} \{ \langle \epsilon_{yy} \rangle_{\Omega}(t) \}} \quad (8)$$

$$M_{22}(\omega) = \frac{\text{FT} \{ \langle \sigma_{yy} \rangle_{\Omega}(t) \}}{\text{FT} \{ \langle \epsilon_{yy} \rangle_{\Omega}(t) \}} \quad (9)$$

$$M_{32}(\omega) = \frac{\text{FT} \{ \langle \sigma_{zz} \rangle_{\Omega}(t) \}}{\text{FT} \{ \langle \epsilon_{yy} \rangle_{\Omega}(t) \}}. \quad (10)$$

Similarly, in a third experiment, a time-varying strain  $\epsilon_{zz}(t)$  is applied on the faces perpendicular to the  $z$  axis with zero strain applied to the other faces which gives

$$M_{13}(\omega) = \frac{\text{FT} \{ \langle \sigma_{xx} \rangle_{\Omega}(t) \}}{\text{FT} \{ \langle \epsilon_{zz} \rangle_{\Omega}(t) \}} \quad (11)$$

$$M_{23}(\omega) = \frac{\text{FT} \{ \langle \sigma_{yy} \rangle_{\Omega}(t) \}}{\text{FT} \{ \langle \epsilon_{zz} \rangle_{\Omega}(t) \}} \quad (12)$$

$$M_{33}(\omega) = \frac{\text{FT} \{ \langle \sigma_{zz} \rangle_{\Omega}(t) \}}{\text{FT} \{ \langle \epsilon_{zz} \rangle_{\Omega}(t) \}}. \quad (13)$$

In order to compute the remaining moduli  $G_1$ ,  $G_2$ , and  $G_3$ , we perform three additional experiments in which a time-varying shear stress  $\sigma_{ij}(t)$  is applied as a traction on the faces of the sample with  $i \neq j$ . The stresses applied normal to the sample's faces are zero, and a sealed boundary condition is again applied to all the

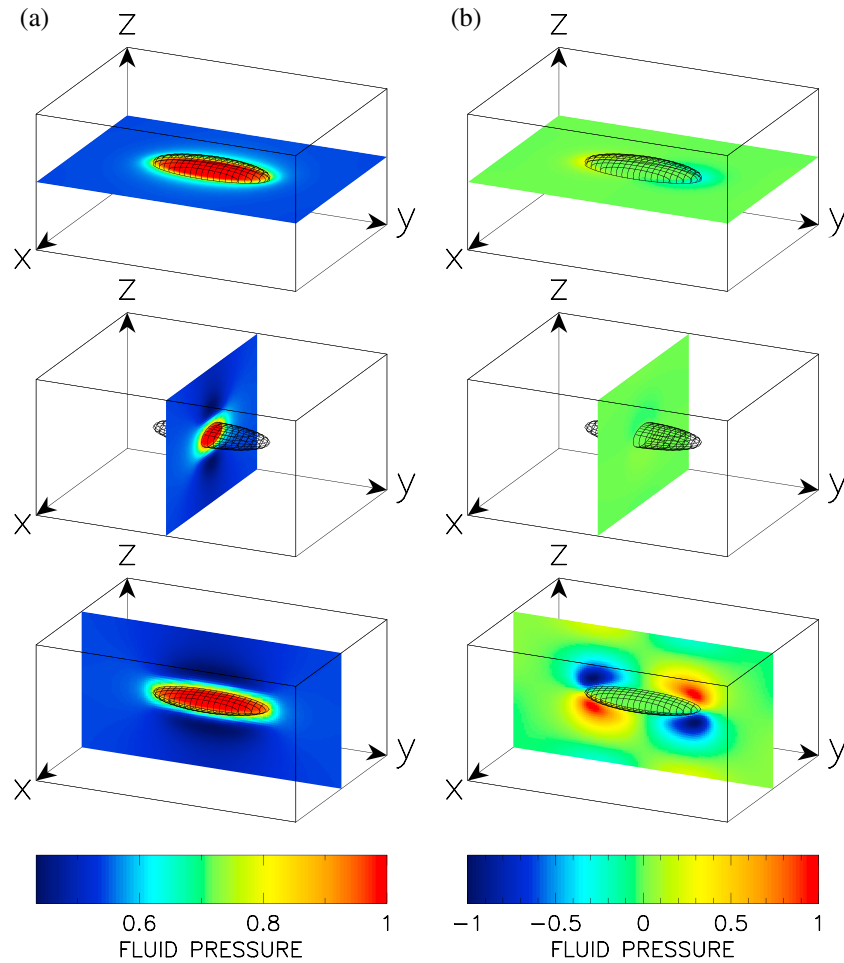


**Figure 1.** Snapshots showing the fluid pressure recorded at early times (a) after a uniaxial compression is applied in the z direction and (b) after a simple shear traction  $\sigma_{yz}$  (with all other stress components zero) is applied to the two faces in the z direction and the two faces in the y direction. The sample consists of a homogeneous matrix containing a single ellipsoidal heterogeneity. In Figure 1a, most of the fluid equilibration occurs between the inclusion and the matrix. In Figure 1b, the fluid pressure equilibrates between the lobes of compression and dilatation induced in the matrix by the heterogeneity. The material properties of the inclusion and matrix are given in Table 1. The horizontal slice in the top of both columns in Figures 1a and 1b was taken a half a grid point below the plane of symmetry of the ellipsoid.

faces. In each experiment, the average strain  $\langle \epsilon_{ij} \rangle_{\Omega}(t)$  induced by the applied stress  $\sigma_{ij}(t)$  is recorded versus time, and the complex  $G_i$  moduli are computed as

$$G_1(\omega) = \frac{\text{FT} \left\{ \langle \sigma_{yz} \rangle_{\Omega}(t) \right\}}{\text{FT} \left\{ \langle \epsilon_{yz} \rangle_{\Omega}(t) \right\}} \quad (14)$$

$$G_2(\omega) = \frac{\text{FT} \left\{ \langle \sigma_{zx} \rangle_{\Omega}(t) \right\}}{\text{FT} \left\{ \langle \epsilon_{zx} \rangle_{\Omega}(t) \right\}} \quad (15)$$

$$G_3(\omega) = \frac{\text{FT} \left\{ \langle \sigma_{xy} \rangle_{\Omega}(t) \right\}}{\text{FT} \left\{ \langle \epsilon_{xy} \rangle_{\Omega}(t) \right\}}. \quad (16)$$

Again, note that these complex shear moduli are related to the complex components of the stiffness tensor as  $G_i = 2C_{jkik}$  where  $i \neq j \neq k$ .

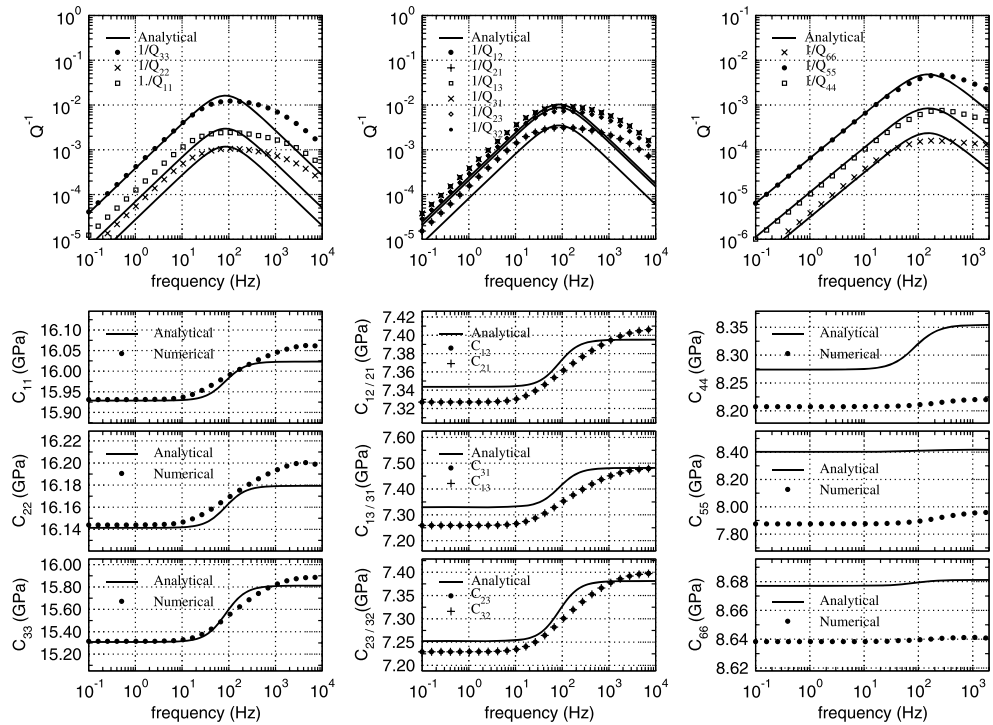


**Figure 2.** Real parts of the nine orthotropic moduli and their respective attenuations obtained for a single weak ellipsoidal heterogeneity embedded within a stiffer homogeneous matrix. The dimensions of the sample are  $L_1 = 31$  mm,  $L_2 = 41$  mm, and  $L_3 = 21$  mm; the dimensions of the ellipsoid are  $l_1 = 10.3$  mm,  $l_2 = 27.3$  mm, and  $l_3 = 4.7$  mm (see Figure 3 for a definition of these parameters). The elastic properties of the matrix and the inclusions are given in Table 1. In all graphs, the points represent numerical results, and solid lines represent results obtained using the analytical expression that is developed in section 3.

Last, the attenuation associated with a given elastic modulus  $C_{ij}$  (where each index runs from 1 to 6 in matrix notation) can be evaluated by computing the inverse quality factor [Masson and Pride, 2007]

$$Q_{C_{ij}}^{-1}(\omega) = -\frac{\text{Im}\{C_{ij}(\omega)\}}{\text{Re}\{C_{ij}(\omega)\}}, \quad (17)$$

where the subscript on  $Q^{-1}$  refers to the modulus (specific stress and strain experiment) from which it has been determined. In Appendix A, we derive in general terms that the ratio of the imaginary to real parts of the elastic moduli is identical to a  $Q^{-1}$  physically defined as the ratio of energy irreversibly lost in each cycle of stressing to the average energy reversibly stored in each cycle (and the result divided by  $4\pi$ ).

#### 4. Numerical Results

In Figure 1, we show that the mesoscale fluid-pressure anomalies that drive the fluid flow can be created in two different ways in fluid-saturated porous samples. On the one hand, when the sample is subject to a global volume change, the fluid pressure response is heterogeneous and correlates with the heterogeneity of the incompressibility within the sample. On the other hand, when the sample is subject to a pure shear stress, an anisotropically shaped mesoscale patch can create lobes of compression and dilation in the material that surrounds it with associated fluid-pressure anomalies.

In Figure 1a, a uniaxial compressional displacement is applied in the  $z$  direction to the upper and lower faces of a rectangular sample (cuboid) containing a single horizontally aligned ellipsoidal heterogeneity in the frame moduli. No displacements are allowed to occur on the faces of the sample in the two horizontal directions. The fluid-pressure response a short instance after the uniaxial deformation is applied is seen to be larger inside the ellipsoid, which has a more compressible frame, than in the surrounding matrix, which has a stiffer frame. The numerical results in this figure are generated using our time-domain poroelastic finite-difference code first given by Masson *et al.* [2006]. As time proceeds, the pressure difference between

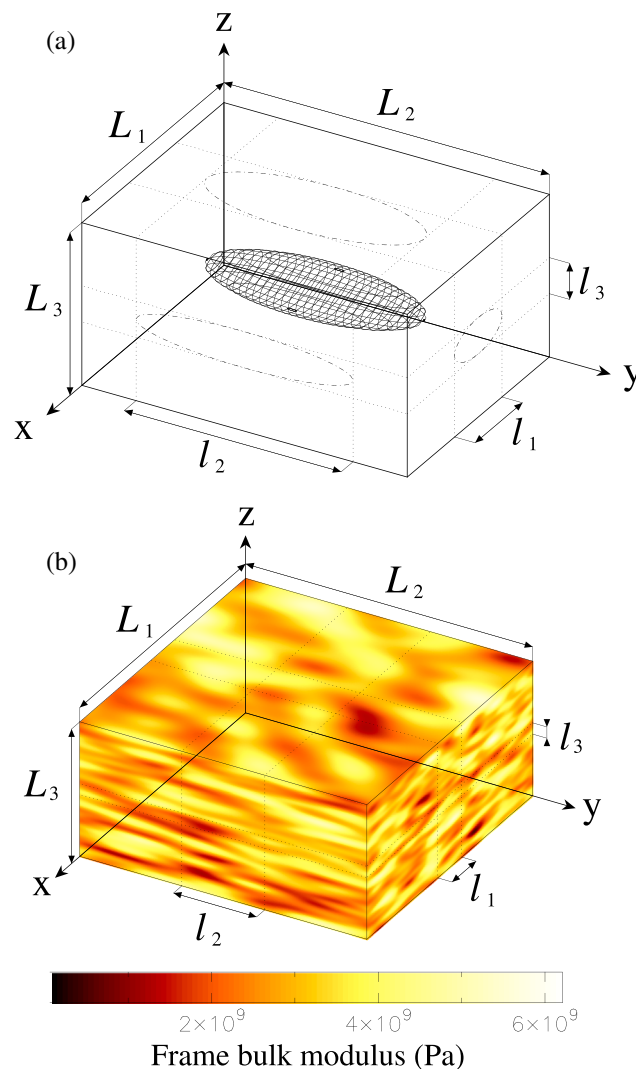


**Figure 3.** An illustration of the two different types of sample geometries used for the numerical experiments. (a) The sample consists of a single ellipsoidal heterogeneity embedded within a homogeneous matrix. (b) The sample is a random material having a different Gaussian correlation function in the three orthogonal directions of space. In both Figures 3a and 3b,  $L_1$ ,  $L_2$ , and  $L_3$  are the sample dimensions in the  $x$ ,  $y$ , and  $z$  directions, respectively. In Figure 3a,  $l_1$ ,  $l_2$ , and  $l_3$  are the main diameters of the ellipsoid. In Figure 3b  $l_1$ ,  $l_2$ , and  $l_3$  correspond to the correlation lengths in the  $x$ ,  $y$ , and  $z$  directions, respectively.

shown in Figure 3a. The analytical results shown as solid lines in the figure will be developed in section 3 and will not be discussed until then. All relaxation and dispersion observed in Figure 2 is due to the mesoscale equilibration of heterogeneity-induced fluid pressure anomalies and has nothing to do with the development of viscous boundary layers in the pores (which is the Biot mechanism of relaxation that occurs at much higher frequencies). The material properties of the matrix and inclusion are given in Table 1.

The attenuation curves presented in the three top panels exhibit some similarities: at low enough frequencies, the attenuation increases linearly with increasing frequency; then, a peak of attenuation is observed; and at high enough frequencies, the attenuation decreases with increasing frequency. Although the shapes of the different attenuation curves are similar, their amplitudes differ. Many studies [see for example *White, 1975; Pride et al., 2004*] have shown that, for regularly spaced heterogeneities of equal size, attenuation is maximum as a function of frequency when the fluid pressure has just enough time to equilibrate between

the ellipsoidal inclusion and the surrounding matrix equilibrates by fluid flow which dissipates energy. This type of deformation-induced fluid flow is the mechanism of attenuation being considered in this study.

In Figure 1b, a tangential shear stress  $\sigma_{yz}$  is applied as a traction to the four sample faces in the  $z$  and  $y$  directions, while displacement is kept at zero on the remaining two faces in the  $x$  direction. In this pure shear case, the overall volume of the sample and hence the average fluid pressure remain constant during the experiment; however, lobes of fluid-pressure anomaly appear in the surrounding material in the first moments after the shear stress is applied. With increasing time, the fluid-pressure differences between the lobes will equilibrate by fluid flow. So pure shear can generate fluid flow through this mechanism in samples with anisotropic poroelastic structure and thus dissipates energy.

Figure 1 clearly emphasizes the fact that the way the fluid-pressure equilibrates within the sample strongly depends on how the sample is deformed or stressed relative to the orientation of the heterogeneity. Consequently, the attenuation levels associated with the different elastic moduli will not necessarily be equal in anisotropic materials.

In Figure 2, we show the real parts of the nine orthotropic moduli and their associated attenuations numerically measured in a sample consisting of a single ellipsoidal inclusion surrounded by a homogeneous matrix as

**Table 1.** Material Properties Used in the Numerical Examples

Property	Phase 1
<i>Matrix</i>	
Grain Bulk modulus ( $K_s$ )	36.0 GPa
Grain density ( $\rho_s$ )	2650 kg/m <sup>3</sup>
Bulk modulus ( $K_d$ )	6.21 GPa
Shear modulus ( $\mu$ )	4.55 GPa
Porosity ( $\phi$ )	0.33
Permeability ( $k$ )	310 <sup>-14</sup> m <sup>2</sup>
<i>Ellipsoid</i>	
Grain Bulk modulus ( $K_s$ )	36.0 GPa
Grain density ( $\rho_s$ )	2650 kg/m <sup>3</sup>
Bulk modulus ( $K_d$ )	62.1 MPa
Shear modulus ( $\mu$ )	45.5 MPa
Porosity ( $\phi$ )	0.33
Permeability ( $k$ )	310 <sup>-14</sup> m <sup>2</sup>
<i>Fluid</i>	
Bulk modulus ( $K_f$ )	2.25 GPa
Density ( $\rho_f$ )	10 <sup>3</sup> kg/m <sup>3</sup>
Viscosity ( $\eta$ )	10 <sup>-3</sup> N s m <sup>-2</sup>

the heterogeneities and the matrix in each wave period. In this case, the relaxation frequency  $\omega_p$  at which the attenuation is maximum is the standard diffusion relation

$$\omega_p = \frac{D}{L^2} \propto \frac{k_0}{L^2}, \quad (18)$$

where  $L$  is the characteristic size of the heterogeneities (a diffusion length) and is explicitly defined for porous patches in Appendix C,  $k_0$  is the permeability, and  $D$  is the fluid-pressure diffusivity. The formal definition of  $D$  is given by *Pride et al.* [2004] or *Pride* [2005], but a simple approximate expression  $D = k_0 K_f / (\eta \phi)$  is sufficient for estimating the timing of diffusion where  $K_f$  is the fluid bulk modulus,  $\eta$  is the fluid viscosity and  $\phi$  is porosity. The numerical results show that all the attenuation curves associated with the  $M_{ij}$  moduli reach their maximum at the same frequency. As the  $M_{ij}$  moduli are obtained using uniaxial compression experiments, pressure equilibration is dominated by the fluid exchange between the heterogeneity and the matrix, and equation (18) gives a good estimate of the frequency at which the maximum attenuation is observed.

The situation is different when the fluid-pressure equilibration occurs between the compressional and dilatational lobes induced in the matrix by stress applied tangentially to the faces of the cuboid. In this case, the position of the attenuation peak depends on the distance between the compressed and the dilated regions and on the permeabilities of both the ellipsoid and the matrix. Thus, the attenuation peaks associated with the  $G_i$  will not necessarily be observed at the same frequency depending on the direction of the applied shear stress and on the elongation of the ellipsoid in the different directions. In the rest of this paper, for well-localized inclusions (i.e., inclusions that are not very elongated or flattened), we consider that the differences between the relaxation frequencies associated with the three  $G_i$  are small.

When both the matrix and heterogeneities are made of homogeneous, isotropic, porous materials, the only way to have anisotropy in the macroscopic moduli of the sample is to have some anisotropy in the shape of the heterogeneity. As we have seen in the previous paragraph, when the inclusion-shape anisotropy is small, similar elastic moduli have about the same relaxation frequency. In this case, it is pertinent to compare their maximum attenuations. In Figure 2, we see that the attenuation observed at the attenuation peak varies greatly depending on the orientation of the ellipsoidal inclusion relative to the direction that strain is applied. Further, the peak attenuation as a function of frequency  $\max [Q_{M_{ij}}^{-1}(\omega)]$  associated with the modulus  $M_{ij}$  increases as the ellipsoid's smallest diameter  $l_i$  becomes less than its largest diameter.

In order to evaluate how the attenuation levels relate to the aspect ratios of the heterogeneities, we perform two series of numerical experiments. The results of these experiments are presented in Figure 4. The first series involves samples containing a single ellipsoidal inclusion embedded in a homogeneous matrix as shown in Figure 3a. The physical properties of the inclusion and the matrix are again given in Table 1. We generate 10 different samples with dimensions

$$L_1 = L_2 = L_3 = 4 \text{ cm} \quad (19)$$

for which the values of the principal diameters of the ellipsoid  $l_1$ ,  $l_2$ , and  $l_3$  are chosen randomly under the conditions that the volume of the ellipsoid is constant

$$v_1 = \frac{4}{3} \pi l_1 l_2 l_3 = 837 \text{ mm}^3 \quad (20)$$

and that the ellipsoid fits within the sample

$$\max [l_1, l_2, l_3] < L_i. \quad (21)$$



For each of the 10 samples, we compute the nine orthotropic moduli in equation (4) and their respective attenuations. We then measure the maximum attenuation associated with each modulus and compute the following ratios:

$$\frac{\max [Q_{M_{ii}}^{-1}(\omega)]}{\max [Q_{M_{jj}}^{-1}(\omega)]} \forall i, j \in [1, 2, 3] \text{ and } i \neq j \quad (22)$$

$$\frac{\max [Q_{M_{ik}}^{-1}(\omega)]}{\max [Q_{M_{jk}}^{-1}(\omega)]} \forall i, j, k \in [1, 2, 3] \text{ and } i \neq j \neq k \quad (23)$$

$$\frac{\max [Q_{G_i}^{-1}(\omega)]}{\max [Q_{G_j}^{-1}(\omega)]} \forall i, j \in [1, 2, 3] \text{ and } i \neq j. \quad (24)$$

In Figure 4 (left column), we plot the three possible attenuation ratios ( $i = 1, j = 2$ ), ( $i = 1, j = 3$ ), and ( $i = 2, j = 3$ ) associated with each of equations (22)–(24) for each of the 10 samples. There are thus 30 points plotted in each panel. We plot them as a function of the aspect ratio  $l_i/l_j$  making sure to use the appropriate index  $i$  and  $j$  corresponding to equations (22)–(24).

The second series of experiments given in Figure 4 (right column) is performed in the same way but using the random property model of Figure 3b. In this case,  $l_1$ ,  $l_2$ , and  $l_3$  denote the correlation lengths of the poroelastic heterogeneity in the  $x$ ,  $y$ , and  $z$  directions, respectively. The poroelastic properties used in the samples are similar to those of the matrix in Table 1 except for the drained bulk and shear moduli. An example of the drained bulk modulus distribution is given by the color scale in Figure 3, and the corresponding distribution for the shear modulus is obtained using  $\mu(x, y, z) = \frac{3}{4}K_d(x, y, z)$ . This choice for the shear modulus corresponds to a dry-frame Poisson ratio of 0.2. For dry sandstones, the Poisson ratio as measured in the laboratory is often close to 0.1 [e.g., *Castagna et al.*, 1985]; however, values in sands and sandstones are sometimes greater than 0.2 and are always greater than 0.2 in carbonate rocks. We feel that choosing 0.2 is a reasonable compromise for representing a range of porous rocks.

For both series of experiments, the numerical results plotted as circles in Figure 4 show a strong linear correlation on the log-log plots which suggests a power law correlation between the attenuation ratios in equations (22)–(24) and the aspect ratios  $l_i/l_j$ . The simple expressions

$$\frac{\max [Q_{M_{ii}}^{-1}(\omega)]}{\max [Q_{M_{jj}}^{-1}(\omega)]} \approx \left( \frac{l_i}{l_j} \right)^{\alpha_1}, \quad (25)$$

$$\frac{\max [Q_{M_{ik}}^{-1}(\omega)]}{\max [Q_{M_{jk}}^{-1}(\omega)]} \approx \left( \frac{l_i}{l_j} \right)^{\alpha_2}, \quad (26)$$

$$\frac{\max [Q_{G_i}^{-1}(\omega)]}{\max [Q_{G_j}^{-1}(\omega)]} \approx \left( \frac{l_i}{l_j} \right)^{\alpha_3} \quad (27)$$

are plotted as solid lines on Figure 4 and fit the numerical data quite well. The proportionality constants in these power laws is 1 because when the aspect ratios are all 1 there is perfect isotropy and the attenuation ratios become 1 as well. We will show in the next section that the discrepancy between the numerical data and equations (25)–(27) is not due to numerical measurement errors, and that the exponents  $\alpha_i$  depend on many parameters.

## 5. Analytical Solution for Peak Attenuation Ratios

The main objective in what follows is to develop an analytical model capable of explaining the attenuation ratios as plotted in Figure 4. Additionally, we will develop an approximate analytical model for the complex frequency-dependent undrained elastic constants of the composite that we now explicitly denote with a subscript  $U$ ;  $C_{ijkl}(\omega) = C_{Uijkl}(\omega)$ . For both tasks, we will need to first obtain models for the real constants  $C_{Dijkl}$  of the dry (no fluid in the pores) composite (these are also the drained moduli of the composite in the low-frequency limit where the fluid pressure everywhere is unchanged by the deformation), the real constants  $C_{Uijkl}(\infty)$  for the undrained moduli at sufficiently high frequencies that no fluid transfer between inclusion and matrix is possible, and the real constants  $C_{Uijkl}(0)$  for the undrained moduli at sufficiently low frequencies that the fluid pressure throughout both the inclusion and matrix is uniform (these latter constants are the so-called *Gassmann* [1951] moduli).

The problem of a mismatched elastic ellipsoid (the inclusion) embedded within an infinite elastic medium (the matrix) subject to remote stress was first solved by *Eshelby* [1957]. His principal result has been extended to the poroelastic case by *Berryman* [1997]. Many authors have used Eshelby's results to derive expressions for the effective anisotropic elastic moduli of elastic composites [see for example *Mori and Tanaka*, 1973; *Benveniste*, 1987; *Maewal*, 1987]. Following the *Mori and Tanaka* [1973] method, *Pan and Weng* [1995] derive explicit expressions for the elastic moduli of heterogeneous elastic composites containing ellipsoidal inclusions and elliptic cracks. Their model for an elastic composite containing aligned ellipsoidal inclusions can be used to estimate the elastic moduli of a dry porous material containing ellipsoidal heterogeneities. We have

$$\mathbf{C}_D^{-1} = (\mathbf{I} + v^{(1)}\mathbf{A}_D^*) : (\mathbf{C}_D^{(0)})^{-1}, \quad (28)$$

where  $\mathbf{C}_D$  is the fourth-order stiffness tensor of the dry porous composite we are modeling (so  $\mathbf{C}_D^{-1}$  is the compliance tensor of the composite),  $\mathbf{C}_D^{(0)}$  is the stiffness tensor of the dry porous matrix surrounding the ellipsoid (superscript 0 is used to denote matrix and 1 to denote inclusion),  $\mathbf{A}_D^*$  is the fourth-order "strain concentration tensor" introduced by *Pan and Weng* [1995],  $v^{(1)}$  is the volume fraction occupied by the ellipsoid, and  $\mathbf{I}$  is the fourth-order symmetric identity tensor defined as  $\mathbf{I} = (1/2)(\delta_{ik}\delta_{jl} + \delta_{il}\delta_{jk})\hat{x}_i\hat{x}_j\hat{x}_k\hat{x}_l$ . For the present case of a dry porous material containing aligned ellipsoidal heterogeneities,  $\mathbf{A}_D^*$  has the expression

$$\mathbf{A}_D^* = [(\mathbf{C}_D^{(1)} - \mathbf{C}_D^{(0)}) : (v^{(1)}\mathbf{I} + v^{(0)}\mathbf{S}) + \mathbf{C}_D^{(0)}]^{-1} : (\mathbf{C}_D^{(1)} - \mathbf{C}_D^{(0)}) \quad (29)$$

where  $\mathbf{C}_D^{(1)}$  is the stiffness tensor of the dry ellipsoidal inclusion,  $\mathbf{S}$  is the fourth-order Eshelby tensor (the components of the Eshelby tensor for ellipsoidal inclusions can be found in Appendix D), and  $v^{(0)} = 1 - v^{(1)}$  is the volume fraction occupied by the matrix. Due to symmetry of an ellipsoid, the composite's dry elastic stiffness tensor  $\mathbf{C}_D$  possesses orthotropic symmetry (nine stiffness components). *Walpole* [1981] provides a methodology for determining the inverse of fourth-order tensors that possess orthotropic symmetry. *Pan and Weng* [1995] perform this considerable algebraic task and give analytical expressions for the nine stiffness components of  $\mathbf{C}_D$  given by equation (28).

In the case where both the ellipsoidal inclusion and the matrix consist of an isotropic porous material, the tensors  $\mathbf{C}_D^{(0)}$  and  $\mathbf{C}_D^{(1)}$  can be expressed in the matrix form

$$\begin{pmatrix} \lambda_D^{(n)} + 2\mu^{(n)} & \lambda_D^{(n)} & \lambda_D^{(n)} & 0 & 0 & 0 \\ \lambda_D^{(n)} & \lambda_D^{(n)} + 2\mu^{(n)} & \lambda_D^{(n)} & 0 & 0 & 0 \\ \lambda_D^{(n)} & \lambda_D^{(n)} & \lambda_D^{(n)} + 2\mu^{(n)} & 0 & 0 & 0 \\ 0 & 0 & 0 & 2\mu^{(n)} & 0 & 0 \\ 0 & 0 & 0 & 0 & 2\mu^{(n)} & 0 \\ 0 & 0 & 0 & 0 & 0 & 2\mu^{(n)} \end{pmatrix} \quad (30)$$

where  $\lambda_D^{(n)} = K_D^{(n)} - \frac{2}{3}\mu^{(n)}$  and where  $K_D^{(n)}$  and  $\mu^{(n)}$  denote the drained bulk moduli and the shear moduli of the porous material composing either the ellipsoids ( $n = 1$ ) or the matrix ( $n = 0$ ).

When the porous composite is saturated with a single fluid and no fluid exchange occurs between the ellipsoids and the matrix (which corresponds to the high-frequency response of the undrained sample), a relation similar to equation (28) can be derived. In this case, we have

$$\mathbf{C}_U^{-1}(\infty) = (\mathbf{I} + v^{(1)}\mathbf{A}_U^*) : (\mathbf{C}_U^{(0)})^{-1} \quad (31)$$

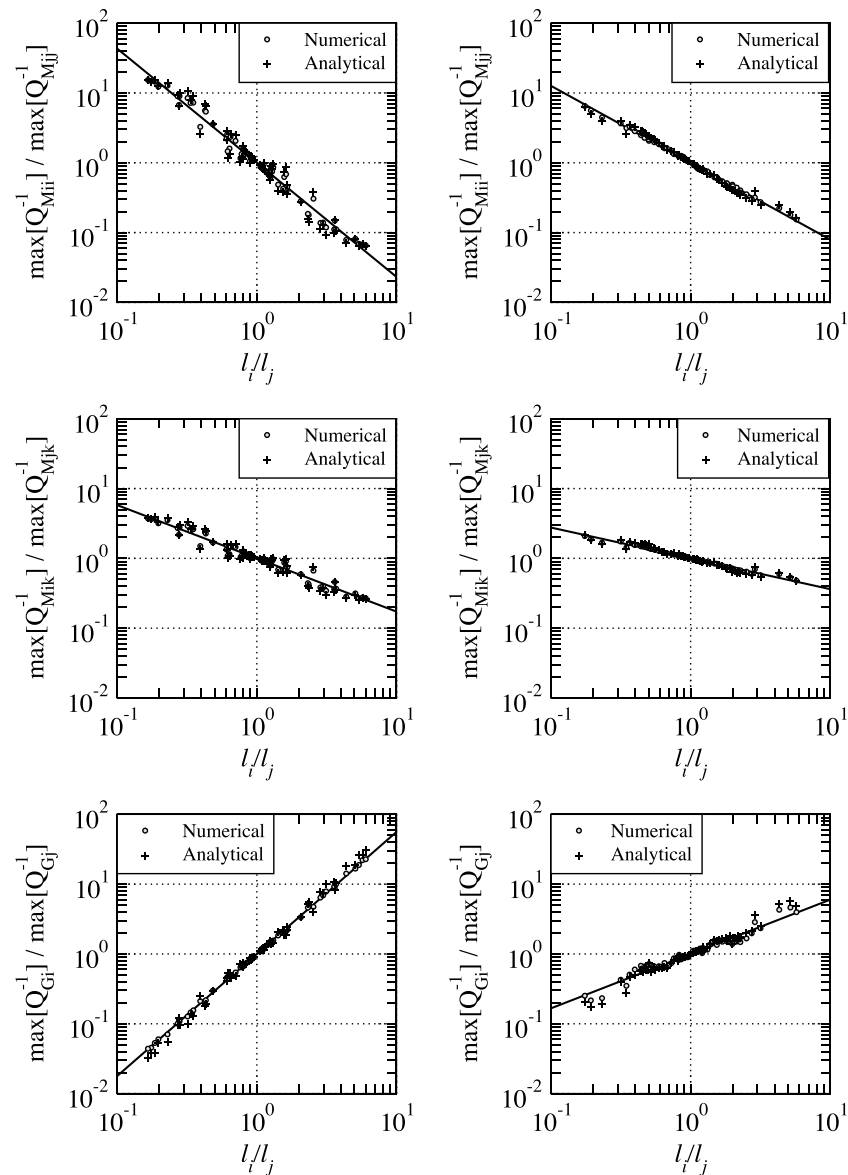


**Figure 4.** Ratios of the maximum attenuations plotted as a function of geometrical aspect ratios. (left column) The results corresponding to 10 different samples containing a single ellipsoidal heterogeneity of different aspect ratios at a fixed inclusion volume fraction of 1.3% (Figure 3a model). The 30 data points seen in each plot correspond to plotting the ratios using the three combinations ( $i = 1, j = 2$ ), ( $i = 1, j = 3$ ), and ( $i = 2, j = 3$ ). (right column) The corresponding results for 10 different realizations of the random Gaussian model (Figure 3b model). The circles correspond to the numerical measurements, and the pluses are the theoretical estimates given by equations (37)–(39).

where  $C_U(\infty)$  is the high-frequency undrained stiffness tensor of the porous composite,  $C_U^{(0)}$  is the undrained stiffness tensor of the matrix, and the undrained eigenstrain concentration tensor  $A_U^*$  is given by the same expression as equation (29) but with subscript  $D$  (drained or dry) replaced everywhere with  $U$  (undrained or sealed). In such an expression for  $A_U^*$ ,  $C_U^{(1)}$  denotes the undrained stiffness tensor of the ellipsoid. If, as we assume, both the inclusions and matrix are locally modeled as being isotropic, the tensors  $C_U^{(n)}$  with  $n = 0, 1$  can again be written in the matrix form of equation (30) after substituting subscript  $D$  everywhere with subscript  $U$ . In this case, the undrained bulk modulus  $K_U^{(n)}$  within each phase is related to the drained modulus of that phase  $K_D^{(n)}$  by the Gassmann [1951] relation given by equation (B9) of Appendix B.

Next, the other famous result of Gassmann [1951] is used to obtain the low-frequency (uniform fluid pressure) undrained fourth-order stiffness tensor  $C_U(0)$  of the composite. Assuming that the framework of grains

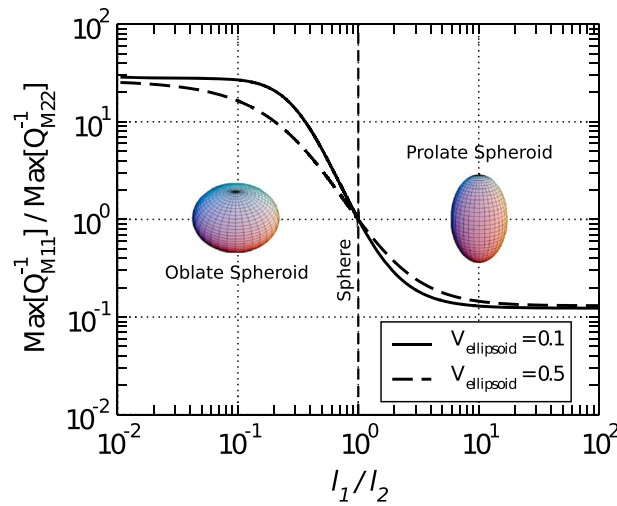


**Figure 5.** Attenuation ratio ( $\max [Q_{M11}^{-1}] / \max [Q_{M22}^{-1}]$ ) computed using equation (37) and plotted as a function of the aspect ratio  $l_1/l_2$  for spheroidal inclusions where  $l_1 \neq l_2 = l_3$ . The properties of the matrix and the ellipsoid are given in Table 1; the black curve corresponds to ellipsoids occupying 10% of the sample's volume, and the dashed curve corresponds to ellipsoids occupying 50% of the sample's volume. We see that when the shape of the inclusion is close to a sphere, the attenuation ratios can be related to the aspect ratios by a power law. When  $l_1$  becomes large, the attenuation ratio reaches a limit corresponding to an infinite cylinder (or needle shape). When  $l_1$  is small, the attenuation ratio reaches a limit corresponding to an infinite flat slab (or penny shape).

form fluid pressure for which Gassmann's theory applies) and very high frequencies (no exchange of fluid between inclusion and matrix).

Using the above results, we next want to construct a model for the complex frequency-dependent undrained bulk modulus  $C_U(\omega)$  over the full range of frequencies. Unfortunately, analytical modeling of how the deformation-induced fluid pressures equilibrate around anisotropically shaped inclusions is a difficult problem that will not be rigorously treated in this paper. We instead make a simple approximation. In the case where the fluid pressure equilibration between the inclusions and the matrix is dominant, and not fluid equilibration between lobes in the matrix surrounding an anisotropically shaped inclusion, it is reasonable to assume that the double porosity theory of *Pride et al.* [2004] captures much of the frequency dependence in the undrained anisotropic moduli. As an approximation, we therefore propose to force the double porosity theory to match the high  $C_U(\infty)$  and low  $C_U(0)$  frequency limits of the anisotropic moduli derived above. This can be achieved using the simple formula

$$C_{Uijkl}(\omega) = C_{Uijkl}(0) + \frac{C_{Uijkl}(\infty) - C_{Uijkl}(0)}{K_U(\infty) - K_U(0)} [K_U(\omega) - K_U(0)] \quad (35)$$

where  $K_U(\omega)$  is the frequency-dependent undrained modulus of the sample computed using the double porosity theory, and  $K_U(\infty)$  and  $K_U(0)$  are its high- and low-frequency limits. Expressions for  $K_U(\infty)$ ,  $K_U(0)$ , and  $K_U(\omega)$  can be found in Appendices B and C.

The estimates of the frequency-dependent undrained elastic moduli  $C_{Uijkl}(\omega)$  (using equation (35)) are presented as the solid lines in Figure 2. We see that this rough derivation of the elastic moduli versus frequency is in reasonable agreement with much of the numerical data. Note that the fit is better for the  $M_{ij}$  moduli, which is due to the fact that the fluid equilibrates mostly between the inclusions and the matrix in this case which is what the double-porosity theory allows for. When looking at the attenuation peaks, we see that the theoretical attenuation levels are in very good agreement with the numerical experiments. The frequency dependence in the attenuation is less accurate due to the assumption that a homogeneous compression (as opposed to an anisotropic applied deformation) is driving the pressure changes and subsequent fluid flow.

within the composite is again made of a single isotropic material characterized by the bulk modulus  $K_s$  and with the dry frame of the composite having the already determined stiffness tensor  $C_D$ , Gassmann [1951] obtained

$$C_{Uijkl}(0) = C_{Dijkl} + \frac{c}{[1 + c/(3K_s)]} \frac{b_{ij}b_{kl}}{(b_{11} + b_{22} + b_{33})} \quad (32)$$

where the  $b_{ij}$  are defined

$$b_{ij} = \delta_{ij} + \frac{C_{D11ij} + C_{D22ij} + C_{D33ij}}{3K_s} \quad (33)$$

with  $\delta_{ij}$  the Kronecker delta function and with  $c$  an auxiliary stiffness given by

$$\frac{1}{c} = \phi \left( \frac{1}{K_f} - \frac{1}{K_s} \right) \quad (34)$$

with  $K_f$  the fluid bulk modulus and  $K_s$  the solid bulk modulus that is assumed here to be the same in both inclusion and matrix.

To summarize, we have so far obtained models of the undrained elastic moduli in the limits of very low frequencies (uni-

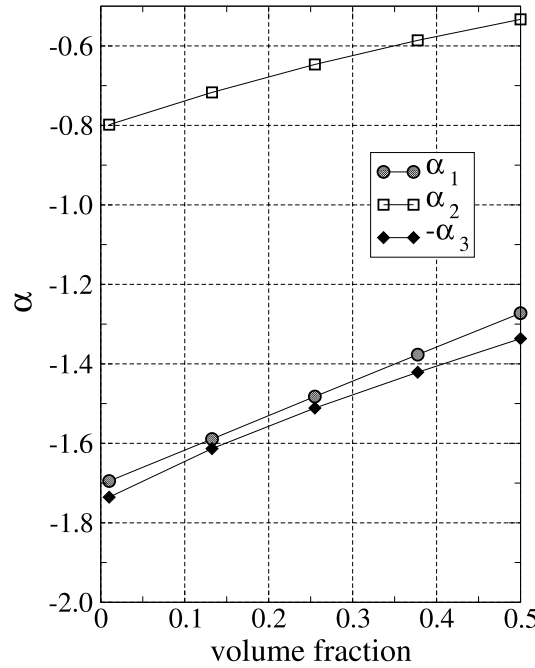


**Figure 6.** The three power law exponents of equations (25)–(27) determined for ellipsoids over the range of aspect ratios  $0.3 < l_i/l_j < 3$  at different volume fractions. There is a definite functional dependence between the exponents and the volume fraction.

$$\frac{\max [Q_{G_i}^{-1}(\omega)]}{\max [Q_{G_j}^{-1}(\omega)]} = \frac{C_{U_{jkjk}}(\infty) - C_{U_{jkjk}}(0)}{C_{U_{ikik}}(\infty) - C_{U_{ikik}}(0)} \quad (39)$$

which is independent of the approximate frequency dependence given by equation (35). Models of  $C_U(\infty)$  and  $C_U(0)$  were given above as equations (31) and (32). In Figure 4, the attenuation ratios computed using equations (37)–(39) are represented by pluses and correlate very well with the ratios computed numerically by finite differences (the circles). We see that the differences between the computed data and the power laws of equations (25)–(27) are not due to numerical errors and can actually be predicted using equations (37)–(39).

Other series of experiments have shown that the power laws of equations (25)–(27) fit the data well only when the anisotropy in the shape of the ellipsoidal inclusion is weak (say, when  $0.3 < l_i/l_j < 3$ ). In Figure 5, we use equation (37) to plot the attenuation ratio for compressional waves over a wide range of aspect ratios. A smooth bijective relation between the attenuation ratio and the aspect ratio is observed for spheroidal inclusions (i.e., when two of the three ellipsoid radii are equal). When the anisotropy is weak, a straight-line slope is observed near  $l_1/l_2 = 1$  which can be taken as the exponent of a power law for a small (weak anisotropy) range of aspect ratios. The exponent of this power law depends, among other things, on the volume fraction occupied by the ellipsoid (as seen in Figure 5).

The reason the curve in Figure 5 for the spheroid is smooth, while similar results plotted as pluses in Figure 4 for ellipsoids slightly deviate from a smooth power law, is that a spheroid has only one aspect ratio while an ellipsoid has three. So if we are plotting, for example,  $\max [Q_1^{-1}]/\max [Q_2^{-1}]$  as a function of  $l_1/l_2$  for an ellipsoid, although the dominate dependence is with  $l_1/l_2$ , the other two aspect ratios  $l_1/l_3$  and  $l_2/l_3$  have a minor influence as well which is largely responsible for the deviations from the smooth power laws seen in Figure 4.

To conclude, we again use equations (37)–(39) to compute the peak attenuation ratios for 30 realizations of ellipsoidal inclusions all corresponding to the same volume fraction but with aspect ratios distributed

Our next task is to compute the peak-attenuation ratios given earlier in Figure 4. Because the attenuation as measured by  $Q^{-1}$  rises linearly to a peak value then falls to zero as frequency increases, the peak attenuation value associated with a given elastic modulus  $C$  will be proportional to the difference between the high  $C(\infty)$  and low  $C(0)$  frequency limits of that modulus, i.e.,

$$\max [Q_C^{-1}(\omega)] = A [C(\infty) - C(0)] \quad (36)$$

where  $A$  is a model-dependent proportionality constant which depends on how the fluid pressure equilibrates within the sample. If we assume that  $A$  is constant for a given group of elastic moduli such as the  $M_{ij}$ , the  $M_{ij}$ , or the  $G_i$ , then the attenuation ratios in equations (22)–(24) can be computed using

$$\frac{\max [Q_{M_{ij}}^{-1}(\omega)]}{\max [Q_{M_{ji}}^{-1}(\omega)]} = \frac{C_{U_{iiii}}(\infty) - C_{U_{iiii}}(0)}{C_{U_{jjjj}}(\infty) - C_{U_{jjjj}}(0)} \quad (37)$$

$$\frac{\max [Q_{M_{ik}}^{-1}(\omega)]}{\max [Q_{M_{jk}}^{-1}(\omega)]} = \frac{C_{U_{iikk}}(\infty) - C_{U_{iikk}}(0)}{C_{U_{jjkk}}(\infty) - C_{U_{jjkk}}(0)} \quad (38)$$

in the range of  $0.3 < l_i/l_j < 3$ . The elastic moduli of the inclusion and host are again those of Table 1. The attenuation ratios so determined, when plotted on a log-log plot as a function of aspect ratio, look very much like Figure 4. The power law exponents of equations (25)–(27) are then determined and plotted in Figure 6 as a function of volume fraction of the inclusion where a nearly linear trend with volume fraction is observed. In addition to the volume fraction, the power law exponents also depend on the elastic moduli of the inclusion and host. So the exponents are far from universal. At this time, we have not attempted to algebraically analyze the Eshelby tensor given in Appendix D in order to extract an analytical understanding for how the power law exponents implicitly contained within equations (37)–(39) at aspect ratios near 1 depend on material properties.

## 6. Conclusions

For the special class of porous materials consisting of aligned ellipsoidal inclusions within a homogeneous matrix, it is possible to relate the poroelastic attenuation associated with the different anisotropic moduli (different modes of deformation) to the geometry of the heterogeneities responsible for this attenuation. We showed this can be achieved without solving the difficult problem of dynamic fluid flow induced when the material is subject to a nonuniform stress or strain. The analytical expressions in our principal result of equations (37)–(39) may perhaps be further developed, in the limit of weak anisotropy, to obtain explicit relations between the attenuation ratios and the aspect ratios of the ellipsoidal inclusions embedded within the Eshelby tensor, but we have not performed that extensive algebraic exercise here. In the special case of weak anisotropy, we have numerically shown that the attenuation ratios are approximately related to the aspect ratios of the ellipsoid by power laws having proportionality constants of 1. The exponents in these power laws do not appear to be universal constants and are observed to vary nearly linearly with the volume fraction of the ellipsoidal inclusions.

There is a practical implication to the fact that the attenuation ratios are correlated to the geometrical aspect ratios of the inclusions or to the correlation lengths of random heterogeneity. By measuring the amplitude ratios of compressional and/or shear waves traveling in different directions, one can imagine deducing the shape and the orientation of the mesoscale heterogeneities present in the propagation medium, i.e., in principal, the lengths  $l_1$ ,  $l_2$ , and  $l_3$  (either inclusion diameters or correlation lengths), as well as the orientation of the anisotropic structure relative to the coordinate axes, could be inverted for from the attenuation ratios using, for example, equations (37)–(39) under the assumption that either the elastic constants of the inclusion and host are known or under the assumption of weak anisotropy.

The ratio of peak compressional wave attenuation to peak shear wave attenuation was not a focus in the present model of ellipsoidal inclusions because these peak attenuations typically occur at different frequencies. For the models presented in this paper, the peak compressional-wave attenuation is typically 3 to 4 times larger than the peak shear-wave attenuation. This is because fluid-pressure equilibration between the ellipsoid and the matrix (compressional waves) produces more attenuation than equilibration between the lobes surrounding the ellipsoid (shear waves). Using an ultrasonic pulse transmission method (frequencies near 1 MHz), *Toksöz et al.* [1979] observe that for a range of sandstones, the shear attenuation is slightly larger than the compressional attenuation. For a transversely isotropic saturated Colorado shale, *Wong et al.* [2008] perform ultrasonic pulse-transmission experiments using compressional and shear waves in various directions and observe that the highest-frequency shear waves are greatly attenuated compared to the compressional waves. Using a resonant bar technique (frequencies near 1 kHz), it can be inferred (after converting the extensional and shear response of a cylindrical sample to the compressional and shear response) that *Murphy* [1982a, 1982b] also observes shear attenuation to be slightly larger than compressional attenuation for Massilon sandstone. So our mechanism of mesoscale fluid flow between lobes of shear-induced fluid pressure change seems to underestimate the shear loss observed in these experiments. The rock samples in these studies likely had fractures in them and shear can create movement of the fluid in the fractures that we have not modeled with our ellipsoidal inclusions.

In numerical results not shown in this paper, we determine the anisotropy in both the attenuation and the moduli for patchy saturation models in which the framework of grains is everywhere uniform, and the immiscible fluid patches are either an ellipsoid, a plane layer, or an invasion cluster created by the Invasion Percolation model [cf. *Wilkinson and Willemsen*, 1983; *Masson and Pride*, 2014]. In all these cases, no significant anisotropy was observed across the seismic band of frequencies (1 to  $10^4$  Hz) despite anisotropy being

present in the fluid patch shapes. Only in the limit of very high frequencies, where the fluid remains in the patches and does not have time to equilibrate, is any anisotropy in the patchy saturation model observed and at such high frequencies there is not much mesoscopic-scale flow and associated attenuation. So the anisotropy in fluid patch shape in patchy saturation models does not lead to significant anisotropy in either the elastic moduli or the associated attenuation.

## Appendix A: Definition of $Q^{-1}$

*O'Connell and Budiansky* [1978] explore a range of definitions of  $Q^{-1}$  that have been used over the years. They obtain the particular result that we derive below as equations (A18) and (A20) but, in doing so, they assume the material to be modeled as a network of springs and dashpots. Our goal here is to derive this result for  $Q^{-1}$  in a way that is applicable to any linear-response system.

Consider some response  $r(t)$  generated by some force  $f(t)$ . In the present paper,  $r(t)$  would be a particular component of stress and  $f(t)$  a particular component of strain, but we do not need to know that here. For linear-response, we have

$$r(t) = \int_{-\infty}^t d\tau M(t - \tau)f(\tau) \quad (\text{A1})$$

where the modulus function  $M(t - \tau)$  is telling us how the force at times past is creating a response at the present time. The chosen limits in the integration is a statement of causality; namely, that response at the present time can only be created by forces at present or past times. By substituting  $u = t - \tau$ , this can also be written

$$r(t) = \int_0^{\infty} du M(u)f(t - u). \quad (\text{A2})$$

We next identify  $\tilde{r}(\omega)$  and  $\tilde{f}(\omega)$  as the Fourier transforms of  $r(t)$  and  $f(t)$

$$\tilde{r}(\omega) = \int_{-\infty}^{\infty} r(t)e^{i\omega t} dt \quad (\text{A3})$$

$$\tilde{f}(\omega) = \int_{-\infty}^{\infty} f(t)e^{i\omega t} dt. \quad (\text{A4})$$

We then write inverse Fourier transforms as

$$r(t) = \frac{1}{2\pi} \int_{-\infty}^{\infty} \tilde{r}(\omega)e^{-i\omega t} d\omega \quad (\text{A5})$$

$$f(t - u) = \frac{1}{2\pi} \int_{-\infty}^{\infty} \tilde{f}(\omega)e^{-i\omega(t-u)} d\omega \quad (\text{A6})$$

and use them in the convolution of equation (A2) to obtain

$$\int_{-\infty}^{\infty} d\omega \tilde{r}(\omega)e^{-i\omega t} = \int_{-\infty}^{\infty} d\omega \left[ \int_0^{\infty} du M(u)e^{i\omega u} \right] \tilde{f}(\omega)e^{-i\omega t}. \quad (\text{A7})$$

We thus have the convolution theorem result that

$$\tilde{r}(\omega) = \tilde{M}(\omega)\tilde{f}(\omega) \quad (\text{A8})$$

where the complex modulus  $\tilde{M}(\omega)$  is defined

$$\tilde{M}(\omega) = \int_0^{\infty} du M(u)e^{i\omega u}. \quad (\text{A9})$$

The fact that the integral is only over positive times is again the statement of causality. As an aside, a straightforward and standard application of Cauchy's theorem that uses the causal form of equation (A9) yields the Kramers-Kronig relations that relate the real and imaginary parts of  $\tilde{M}(\omega)$  as Hilbert transform pairs [e.g., *Landau and Lifshitz*, 1980].

The linear-response system is now assumed to be driven by a sinusoidal force at a frequency  $\omega$  so that

$$f(t) = \text{Re} \{ f_o e^{-i\omega t} \} = \frac{1}{2} [f_o e^{-i\omega t} + f_o^* e^{i\omega t}] \quad (\text{A10})$$

$$r(t) = \text{Re} \{ \tilde{M}(\omega) f_o e^{-i\omega t} \} = \frac{1}{2} [\tilde{M}(\omega) f_o e^{-i\omega t} + \tilde{M}(\omega)^* f_o^* e^{i\omega t}]. \quad (\text{A11})$$

Focus is put on the stored energy  $E(t)$  of the response defined as

$$E(t) = r(t)f(t) \quad (\text{A12})$$

$$= \frac{1}{4} [2\tilde{M}_R f_o f_o^* + \tilde{M} f_o^2 e^{-2i\omega t} + \tilde{M}^* f_o^{*2} e^{2i\omega t}] \quad (\text{A13})$$

where we have written  $\tilde{M} = \tilde{M}_R + i\tilde{M}_I$  so that  $\tilde{M} + \tilde{M}^* = 2\tilde{M}_R$ . The rate at which energy is changing is given by

$$\frac{dE(t)}{dt} = \frac{dr(t)}{dt} f(t) + r(t) \frac{df(t)}{dt} \quad (\text{A14})$$

$$= \omega \tilde{M}_I f_o f_o^* - \frac{i\omega}{2} \tilde{M} f_o^2 e^{-2i\omega t} + \frac{i\omega}{2} \tilde{M}^* f_o^{*2} e^{2i\omega t} \quad (\text{A15})$$

where we have used that  $\tilde{M} - \tilde{M}^* = 2i\tilde{M}_I$ .

Next, the total energy dissipated over one period  $T = 2\pi/\omega$  is determined

$$D = \int_0^T dt \frac{dE(t)}{dt} = 2\pi \tilde{M}_I f_o f_o^* \quad (\text{A16})$$

where the integrals involving  $e^{\pm 2i\omega t}$  are zero over  $[0, T]$ . Thus, the net energy change added up over each period is controlled entirely by  $\tilde{M}_I$ . The energy change given by  $D$  will always be negative because stored energy is lost to heat which means that  $\tilde{M}_I$  is negative. The average energy reversibly stored in each cycle is given by

$$E_{\text{ave}} = \frac{1}{T} \int_0^T dt E(t) = \frac{\tilde{M}_R}{2} f_o f_o^* \quad (\text{A17})$$

where again the integrals involving  $e^{\pm 2i\omega t}$  are zero. The average energy stored during each cycle is controlled entirely by  $\tilde{M}_R$  and is always positive.

A convenient measure of loss is therefore the dimensionless quality factor  $Q(\omega)$  defined as

$$\frac{1}{Q(\omega)} = \frac{\text{energy dissipated over one cycle}}{(4\pi)(\text{average energy stored in each cycle})} \quad (\text{A18})$$

$$= \frac{-D}{4\pi E_{\text{ave}}} \quad (\text{A19})$$

$$= -\frac{\tilde{M}_I(\omega)}{\tilde{M}_R(\omega)}. \quad (\text{A20})$$

Other definitions of  $Q(\omega)$  exist for defining loss, but the above seems to be the most useful and convenient.

## Appendix B: The Biot Model

*Biot* [1962] equations are used to model the local response within a heterogeneous porous sample that is being stressed in a time-varying manner. As demonstrated by *Masson et al.* [2006], at low enough applied frequencies where  $\omega \ll \eta / (\rho_f Fk)$  so that viscous boundary layers do not develop in the pores, *Biot* [1962] equations in the time domain may be written

$$\rho \frac{\partial \mathbf{v}}{\partial t} = \nabla \cdot \boldsymbol{\tau} - \rho_f \frac{\partial \mathbf{q}}{\partial t} \quad (\text{B1})$$

$$\rho_f (1 + \Phi) F \frac{\partial \mathbf{q}}{\partial t} + \frac{\eta}{k_0} \mathbf{q} = -\nabla p - \rho_f \frac{\partial \mathbf{v}}{\partial t}. \quad (\text{B2})$$

$$\frac{\partial \boldsymbol{\tau}}{\partial t} = (\lambda_U \nabla \cdot \mathbf{v} + \alpha M \nabla \cdot \mathbf{q}) \mathbf{I} + \mu [\nabla \mathbf{v} + (\nabla \mathbf{v})^T] \quad (\text{B3})$$



$$-\frac{\partial p}{\partial t} = M(\alpha \nabla \cdot \mathbf{v} + \nabla \cdot \mathbf{q}). \quad (\text{B4})$$

In sedimentary rocks, these equations can be considered as valid across the seismic band (1 to  $10^4$  Hz). The various coefficients are all real. Here  $\rho$  is the local bulk density of the material,  $\rho_f$  is the fluid density which is taken to be spatially uniform throughout each sample, and  $F$  is the electrical formation factor that is modeled here using the *Archie* [1942] law  $\phi^{-1.75}$ , where  $\phi$  is local porosity and  $\Phi$  is a dimensionless pore-topology parameter defined and discussed by *Masson et al.* [2006] that is bounded as  $\Phi > 1/4$  and will simply be set to 1 in the present article. Over the seismic band of frequencies, the inertial term in the generalized Darcy law of equation (B2) has a magnitude  $|\rho_f(1 + \Phi)F\partial\mathbf{q}/\partial t|$  that is always negligible in amplitude relative to the viscous resistance  $|(\eta/k_o)\mathbf{q}|$ ; however, the inertial term is entirely responsible for the finite-difference scheme to be stable [cf. *Masson et al.*, 2006] and thus cannot be discarded.

The local poroelastic constants used here are the undrained Lamé modulus  $\lambda_U$ , the shear modulus  $\mu$  (the same for both drained and undrained conditions), the so-called *Biot and Willis* [1957] constant  $\alpha$ , and the fluid-storage coefficient  $M$ . For any porous material, these constants are related to the undrained bulk modulus  $K_U$ , the drained bulk modulus  $K_D$  and *Skempton's* [1954] undrained fluid-pressure to confining-pressure ratio  $B$  as

$$\lambda_U = K_U - 2\mu/3 = K_D + \alpha^2 M - 2\mu/3 \quad (\text{B5})$$

$$\alpha = (1 - K_D/K_U)/B \quad (\text{B6})$$

$$M = BK_U/\alpha. \quad (\text{B7})$$

In the special case considered by *Gassmann* [1951], in which the solid frame is composed of a single isotropic mineral characterized by a bulk modulus  $K_s$ , we have as well the so-called “fluid-substitution” relations given by

$$B = \frac{1/K_D - 1/K_s}{1/K_D - 1/K_s + \phi(1/K_f - 1/K_s)} \quad (\text{B8})$$

$$K_U = \frac{K_D}{1 - B(1 - K_D/K_s)} \quad (\text{B9})$$

where  $K_f$  is the fluid bulk modulus and  $\phi$  is the porosity. From these, one further obtains  $\alpha = 1 - K_D/K_s$ . We use the *Gassmann* expressions to model the local poroelastic constants in all the numerical experiments.

### Appendix C: The Double Porosity Model

In the special case where the sample is a composite of two distinct porous materials saturated by a single fluid and when the heterogeneity has a single dominant length scale, the double-porosity theory of *Pride and Berryman* [2003a, 2003b] is applicable and predicts that the undrained bulk modulus  $K_U(\omega)$  of the porous composite is complex (due to the mesoscale fluid equilibration) and given by

$$\frac{1}{K_d(\omega)} = a_{11} - \frac{a_{13}^2}{a_{33} - \gamma/i\omega}, \quad (\text{C1})$$

$$B(\omega) = \frac{-a_{12}(a_{33} - \gamma/i\omega) + a_{13}(a_{23} + \gamma/i\omega)}{(a_{22} - \gamma/i\omega)(a_{33} - \gamma/i\omega) - (a_{23} + \gamma/i\omega)^2}, \quad (\text{C2})$$

$$\frac{1}{K_U(\omega)} = \frac{1}{K_d(\omega)} + B(\omega) \left( a_{12} - \frac{a_{13}(a_{23} + \gamma/i\omega)}{a_{33} - \gamma/i\omega} \right). \quad (\text{C3})$$

Here  $K_d(\omega)$  is the complex drained bulk modulus of the composite (drained in this context means that the average fluid pressure in a sample does not change, which in no way prevents mesoflow from occurring), and  $B(\omega)$  is the complex *Skempton's* coefficient. The *Skempton's* coefficient is the ratio of the average fluid pressure in the composite to an applied confining pressure for a sealed sample and is frequency dependent in the double-porosity model due to mesoflow associated with the heterogeneity in the sample. The  $a_{ij}$

are real elastic compliances that depend on the elastic moduli of the two porous constituents, while  $\gamma$  is a complex function of frequency given by

$$\gamma(\omega) = \gamma_o \sqrt{1 - i \frac{\omega}{\omega_o}} \quad (C4)$$

that controls the degree of mesoflow between the two phases. Expressions for the real parameters  $\gamma_o$  and  $\omega_o$ , as well as for the high-frequency elastic compliances  $a_{ij}$ , have been derived by *Pride and Berryman* [2003a, 2003b] and are also given by *Pride et al.* [2004]. The  $a_{ij}$  are given by

$$a_{11} = 1/K_d(0) \quad (C5)$$

$$a_{22} = \frac{v_1 \alpha_1}{K_1} \left( \frac{1}{B_1} - \frac{\alpha_1(1 - Q_1)}{1 - K_1/K_2} \right) \quad (C6)$$

$$a_{33} = \frac{v_2 \alpha_2}{K_2} \left( \frac{1}{B_2} - \frac{\alpha_2(1 - Q_2)}{1 - K_2/K_1} \right) \quad (C7)$$

$$a_{12} = -v_1 Q_1 \alpha_1 / K_1 \quad (C8)$$

$$a_{13} = -v_2 Q_2 \alpha_2 / K_2 \quad (C9)$$

$$a_{23} = -\frac{\alpha_1 \alpha_2 K_1 / K_2}{(1 - K_1 / K_2)^2} \left( \frac{1}{K_d(0)} - \frac{v_1}{K_1} - \frac{v_2}{K_2} \right) \quad (C10)$$

where

$$v_1 Q_1 = \frac{1 - K_2 / K_d(0)}{1 - K_2 / K_1} \text{ and } v_2 Q_2 = \frac{1 - K_1 / K_d(0)}{1 - K_1 / K_2}. \quad (C11)$$

Here  $v_i$  is the volume-fraction of phase  $i$  in each sample ( $v_1 + v_2 = 1$ ),  $K_i$  is the drained frame modulus of phase  $i$ ,  $B_i$  is the Skempton's coefficient of phase  $i$ , and  $\alpha_i$  is the Biot-Willis constant of phase  $i$ .

The one parameter in these  $a_{ij}$  that has not yet been modeled is the overall static drained modulus  $K_d(0) = 1/a_{11}$  of the two-phase composite. It is through  $K_d(0)$  that all dependence on the mesoscopic geometry of the two phases occurs. Although many mixture models for  $K_d(0)$  exist, none are exact for arbitrary geometry of the inclusions. In the present paper, we numerically calculate  $K_d(0)$  using our finite-difference scheme in the long-time limit and use this measured drained bulk modulus in the above double-porosity expressions for all "theoretical" predictions.

The low-frequency and high-frequency limits of  $K_u(\omega)$  are determined from equation (C4) to be

$$K_u(0) = a_{11} - \frac{(a_{12} + a_{13})^2}{a_{22} + 2a_{23} + a_{33}} \quad (C12)$$

$$K_u(\infty) = a_{11} - \frac{a_{13}^2}{a_{33}} - \frac{(a_{12}a_{33} - a_{13}a_{23})^2}{a_{33}(a_{22}a_{33} - a_{23}^2)}. \quad (C13)$$

At peak attenuation defined when  $\omega = \omega_p$  one can approximate that  $K_u(\omega_p) \approx [K_u(0) + K_u(\infty)]/2$ .

If phase 2 is defined to be more permeable than phase 1, the low-frequency limit of the internal transport coefficient  $\gamma_o$  is given by

$$\gamma_o = -\frac{k_1 K_1^d}{\eta L_1^2} \left( \frac{a_{12} + B_o(a_{22} + a_{33})}{R_1 - B_o/B_1} \right) [1 + O(k_1/k_2)], \quad (C14)$$

where the parameters  $B_o$ ,  $R_1$ , and  $L_1$  are now defined. The dimensionless number  $B_o = B(0)$  is the static Skempton's coefficient for the composite and is exactly

$$B_o = -\frac{(a_{12} + a_{13})}{a_{22} + 2a_{23} + a_{33}}. \quad (C15)$$

The dimensionless number  $R_1$  is the ratio of the average static confining pressure in the host phase 1 of a sealed sample divided by the confining pressure applied to the sample and is exactly

$$R_1 = Q_1 + \frac{\alpha_1(1 - Q_1)B_o}{1 - K_1^d/K_2^d} - \frac{v_2 \alpha_2(1 - Q_2)B_o}{v_1 (1 - K_2^d/K_1^d)} \quad (C16)$$

where the  $Q_i$  are given by equation (C11). Last, the length  $L_1$  is the distance over which the fluid-pressure gradient still exists in phase 1 in the final approach to fluid-pressure equilibrium and is formally defined as

$$L_1^2 = \frac{1}{V_1} \int_{\Omega_1} \Phi_1 dV \quad (C17)$$

where  $\Omega_1$  is the region of an averaging volume occupied by phase 1 and having a volume measure  $V_1$ . The potential  $\Phi_1$  has units of length squared and is a solution of an elliptic boundary-value problem that under conditions where the permeability ratio  $k_1/k_2$  can be considered small, reduces to

$$\nabla^2 \Phi_1 = -1 \text{ in } \Omega_1, \quad (C18)$$

$$\mathbf{n} \cdot \nabla \Phi_1 = 0 \text{ on } \partial E_1, \quad (C19)$$

$$\Phi_1 = 0 \text{ on } \partial \Omega_{12} \quad (C20)$$

where  $\partial \Omega_{12}$  is the surface separating the two phases within a sample of composite and  $\partial E_1$  is the external surface of the sample that is coincident with phase 1.

In all the examples of the present paper, the boundary-value problem for  $\Phi_1$  is solved numerically by finite-differences. To do so, we add a diffusion term  $-\partial \Phi_1 / \partial t$  to the left-hand side of equation (C18) and replace 1 by a step function on the right-hand side, then solve the resulting diffusion equation using explicit time stepping. The long-time steady state response to the imposed step-function source term is the solution of equation (C18). We then determine numerically the length  $L_1$  using equation (C17).

Last, the transition frequency  $\omega_o$  corresponds to the onset of a high-frequency regime in which the fluid-pressure-diffusion penetration distance becomes small relative to the scale of the mesoscopic heterogeneity and is given by

$$\omega_o = \frac{\eta B_1 K_1}{k_1 \alpha_1} \left( \gamma_o \frac{V}{S} \right)^2 \left( 1 + \sqrt{\frac{k_1 B_2 K_2 \alpha_1}{k_2 B_1 K_1 \alpha_2}} \right)^2 \quad (C21)$$

where  $S$  is the surface area of the interface between the two phases in each volume  $V$  of composite.

## Appendix D: The Eshelby Tensor

The derivation of the Eshelby tensor in isotropic materials was initially performed by *Eshelby* [1957] and is also presented by *Mura* [1982]. For isotropic medium, the Eshelby tensor can be expressed in terms of elliptic integrals. Assuming that  $a_1 > a_2 > a_3$  and that the semiaxis  $a_1$ ,  $a_2$ , and  $a_3$  aligns with the coordinate  $x$ ,  $y$ , and  $z$ , respectively, then

$$S_{1111} = \frac{3a_1^2}{8\pi(1-\nu)} I_{11} + \frac{1-2\nu}{8\pi(1-\nu)} I_1 \quad (D1)$$

$$S_{1122} = \frac{3a_2^2}{8\pi(1-\nu)} I_{12} - \frac{1-2\nu}{8\pi(1-\nu)} I_1 \quad (D2)$$

$$S_{1133} = \frac{3a_3^2}{8\pi(1-\nu)} I_{13} - \frac{1-2\nu}{8\pi(1-\nu)} I_1 \quad (D3)$$

$$S_{1212} = \frac{3(a_1^2 + a_2^2)}{16\pi(1-\nu)} I_{12} + \frac{1-2\nu}{16\pi(1-\nu)} (I_1 + I_2) \quad (D4)$$

$$S_{3333} = \frac{3a_3^2}{8\pi(1-\nu)} I_{33} + \frac{1-2\nu}{8\pi(1-\nu)} I_3 \quad (D5)$$

$$S_{3311} = \frac{3a_1^2}{8\pi(1-\nu)} I_{31} - \frac{1-2\nu}{8\pi(1-\nu)} I_3 \quad (D6)$$

$$S_{3322} = \frac{3a_2^2}{8\pi(1-\nu)} I_{32} - \frac{1-2\nu}{8\pi(1-\nu)} I_3 \quad (D7)$$

$$S_{3131} = \frac{3(a_3^2 + a_1^2)}{16\pi(1-\nu)} I_{31} + \frac{1-2\nu}{16\pi(1-\nu)} (I_3 + I_1) \quad (D8)$$

$$S_{2222} = \frac{3a_2^2}{8\pi(1-\nu)} I_{22} + \frac{1-2\nu}{8\pi(1-\nu)} I_2 \quad (D9)$$

$$S_{2233} = \frac{3a_3^2}{8\pi(1-\nu)} I_{23} - \frac{1-2\nu}{8\pi(1-\nu)} I_2 \quad (D10)$$

$$S_{2211} = \frac{3a_1^2}{8\pi(1-\nu)} I_{21} - \frac{1-2\nu}{8\pi(1-\nu)} I_2 \quad (D11)$$

$$S_{2323} = \frac{3(a_2^2 + a_3^2)}{16\pi(1-\nu)} I_{23} + \frac{1-2\nu}{16\pi(1-\nu)} (I_2 + I_3) \quad (D12)$$

The rest of the terms are equal to zero. The  $I_i$  terms are defined in terms of standard elliptic integrals,

$$I_1 = \frac{4\pi a_1 a_2 a_3}{(a_1^2 - a_2^2) \sqrt{a_1^2 - a_3^2}} (F - E) \quad (D13)$$

$$I_3 = \frac{4\pi a_1 a_2 a_3}{(a_2^2 - a_3^2) \sqrt{a_1^2 - a_3^2}} \left( \frac{a_2 \sqrt{a_1^2 - a_3^2}}{a_1 a_3} - E \right) \quad (D14)$$

$$I_2 = 4\pi - I_1 - I_3 \quad (D15)$$

where the  $I_{ij}$  terms are

$$I_{12} = \frac{I_2 - I_1}{3(a_1^2 - a_2^2)} \quad (D16)$$

$$I_{21} = \frac{I_1 - I_2}{3(a_2^2 - a_1^2)} \quad (D17)$$

$$I_{13} = \frac{I_3 - I_1}{3(a_1^2 - a_3^2)} \quad (D18)$$

$$I_{31} = \frac{I_1 - I_3}{3(a_3^2 - a_1^2)} \quad (D19)$$

$$I_{23} = \frac{I_3 - I_2}{3(a_2^2 - a_3^2)} \quad (D20)$$

$$I_{32} = \frac{I_2 - I_3}{3(a_3^2 - a_2^2)} \quad (D21)$$

$$I_{11} = \frac{4\pi}{3a_1^2} - I_{12} - I_{13} \quad (D22)$$

$$I_{22} = \frac{4\pi}{3a_2^2} - I_{23} - I_{21} \quad (D23)$$

$$I_{33} = \frac{4\pi}{3a_3^2} - I_{31} - I_{32} \quad (D24)$$

and the standard elliptic integrals  $F(\theta, k)$  and  $E(\theta, k)$  have the following definition:

$$E(\theta, k) = \int_0^\theta (1 - k^2 \sin^2 w)^{\frac{1}{2}} dw \quad (D25)$$

$$F(\theta, k) = \int_0^\theta \frac{dw}{(1 - k^2 \sin^2 w)^{\frac{1}{2}}} \quad (D26)$$

where

$$\theta = \sin^{-1} \left( \sqrt{1 - \frac{a_3^2}{a_1^2}} \right) \quad (D27)$$

$$k = \sqrt{\frac{a_1^2 - a_2^2}{a_1^2 - a_3^2}}. \quad (D28)$$

In the special case of an oblate spheroid ( $a_1 = a_2 > a_3$ ), the  $l_i$  terms reduce to

$$l_1 = \frac{2\pi a_1 a_2 a_3}{(a_1^2 - a_3^2)^{\frac{3}{2}}} \left[ \cos^{-1} \left( \frac{a_3}{a_1} \right) - \frac{a_3}{a_1} \sqrt{1 - \frac{a_3^2}{a_1^2}} \right] \quad (D29)$$

$$l_2 = l_1 \quad (D30)$$

$$l_3 = \frac{4\pi a_1 a_2 a_3}{(a_2^2 - a_3^2) \sqrt{a_1^2 - a_3^2}} \left( \frac{a_2 \sqrt{a_1^2 - a_3^2}}{a_1 a_3} - E \right) \quad (D31)$$

where

$$l_{13} = \frac{l_3 - l_1}{3(a_1^2 - a_3^2)} \quad (D32)$$

$$l_{31} = \frac{l_1 - l_3}{3(a_3^2 - a_1^2)} \quad (D33)$$

$$l_{23} = \frac{l_3 - l_2}{3(a_2^2 - a_3^2)} \quad (D34)$$

$$l_{32} = \frac{l_2 - l_3}{3(a_3^2 - a_2^2)} \quad (D35)$$

$$l_{12} = \frac{\pi}{3a_1^2} - \frac{l_{13}}{4} \quad (D36)$$

$$l_{21} = l_{12} \quad (D37)$$

$$l_{11} = \frac{4\pi}{3a_1^2} - l_{12} - l_{13} \quad (D38)$$

$$l_{22} = \frac{4\pi}{3a_2^2} - l_{23} - l_{21} \quad (D39)$$

$$l_{33} = \frac{4\pi}{3a_3^2} - l_{31} - l_{32}. \quad (D40)$$

For a prolate spheroid ( $a_1 > a_2 = a_3$ ), the  $l_i$  terms reduce to

$$l_1 = \frac{4\pi a_1 a_2 a_3}{(a_1^2 - a_2^2) \sqrt{a_1^2 - a_3^2}} (F - E) \quad (D41)$$

$$l_2 = \frac{2\pi a_1 a_2 a_3}{(a_1^2 - a_3^2)^{\frac{3}{2}}} \times \left[ \frac{a_1}{a_3} \sqrt{\left( \frac{a_1^2}{a_3^2} - 1 \right)} - \cosh^{-1} \left( \frac{a_1}{a_3} \right) \right] \quad (D42)$$

$$l_3 = l_2 \quad (D43)$$

where

$$l_{12} = \frac{l_2 - l_1}{3(a_1^2 - a_2^2)} \quad (D44)$$

$$l_{21} = \frac{l_1 - l_2}{3(a_2^2 - a_1^2)} \quad (D45)$$

$$l_{13} = \frac{l_3 - l_1}{3(a_1^2 - a_3^2)} \quad (D46)$$

$$l_{31} = \frac{l_1 - l_3}{3(a_3^2 - a_1^2)} \quad (D47)$$

$$l_{23} = \frac{\pi}{3a_2^2} - \frac{l_{21}}{4} \quad (D48)$$

$$l_{32} = l_{23} \quad (D49)$$

$$l_{11} = \frac{4\pi}{3a_1^2} - l_{12} - l_{13} \quad (D50)$$

$$l_{22} = \frac{4\pi}{3a_2^2} - l_{23} - l_{21} \quad (D51)$$

$$l_{33} = \frac{4\pi}{3a_3^2} - l_{31} - l_{32} \quad (D52)$$

For a spherical inclusion, the Eshelby tensor has the simple form

$$S_{1111} = \frac{7 - 5\nu}{15(1 - \nu)} \quad (D53)$$

$$S_{2222} = S_{1111} \quad (D54)$$

$$S_{3333} = S_{1111} \quad (D55)$$

$$S_{1212} = \frac{4 - 5\nu}{15(1 - \nu)} \quad (D56)$$

$$S_{2323} = S_{1212} \quad (D57)$$

$$S_{3131} = S_{1212} \quad (D58)$$

$$S_{1122} = \frac{5\nu - 1}{15(1 - \nu)} \quad (D59)$$

$$S_{2233} = S_{1122} \quad (D60)$$

$$S_{3311} = S_{1122} \quad (D61)$$

$$S_{1133} = S_{1122} \quad (D62)$$

$$S_{2211} = S_{1122} \quad (D63)$$

$$S_{3322} = S_{1122} \quad (D64)$$

while for an infinite cylinder ( $a_3 \rightarrow \infty$ ), we have

$$S_{1111} = \frac{1}{2(1 - \nu)} \times \left( \frac{a_2^2 + 2a_1a_2}{(a_1 + a_2)^2} + (1 - 2\nu) \frac{a_2}{a_1 + a_2} \right) \quad (D65)$$

$$S_{2222} = \frac{1}{2(1 - \nu)} \times \left( \frac{a_1^2 + 2a_1a_2}{(a_1 + a_2)^2} + (1 - 2\nu) \frac{a_1}{a_1 + a_2} \right) \quad (D66)$$

$$S_{3333} = 0 \quad (D67)$$

$$S_{1122} = \frac{1}{2(1 - \nu)} \times \left( \frac{a_2^2}{(a_1 + a_2)^2} - (1 - 2\nu) \frac{a_2}{a_1 + a_2} \right) \quad (D68)$$

$$S_{2233} = \frac{1}{2(1 - \nu)} \frac{2\nu a_1}{a_1 + a_2} \quad (D69)$$

$$S_{2211} = \frac{1}{2(1 - \nu)} \times \left( \frac{a_1^2}{(a_1 + a_2)^2} - (1 - 2\nu) \frac{a_1}{a_1 + a_2} \right) \quad (D70)$$

$$S_{3311} = 0 \quad (D71)$$

$$S_{3322} = 0 \quad (D72)$$

$$S_{1212} = \frac{1}{2(1-\nu)} \left( \frac{a_1^2 + a_2^2}{2(a_1 + a_2)^2} + \frac{1-2\nu}{2} \right) \quad (D73)$$

$$S_{1133} = \frac{1}{2(1-\nu)} \frac{2\nu a_2}{a_1 + a_2} \quad (D74)$$

$$S_{2323} = \frac{a_1}{2(a_1 + a_2)} \quad (D75)$$

$$S_{3131} = \frac{a_2}{2(a_1 + a_2)}. \quad (D76)$$

Finally, the simplified matrix form  $S_{ij}$  of the Eshelby tensor  $S_{ijkl}$  is

$$S_{ij} = \begin{pmatrix} S_{1111} & S_{1122} & S_{1133} & 0 & 0 & 0 \\ S_{2211} & S_{2222} & S_{2233} & 0 & 0 & 0 \\ S_{3311} & S_{3322} & S_{3333} & 0 & 0 & 0 \\ 0 & 0 & 0 & 2S_{1212} & 0 & 0 \\ 0 & 0 & 0 & 0 & 2S_{3131} & 0 \\ 0 & 0 & 0 & 0 & 0 & 2S_{2323} \end{pmatrix}. \quad (D77)$$

#### Acknowledgments

This work was performed under the auspices of the U.S. Department of Energy and supported specifically by the Geosciences Research Program of the DOE Office of Basic Energy Sciences, Division of Chemical Sciences, Geosciences, and Biosciences BES, contract DEACO205CH11231. Y. Masson has recently been supported through the European Union's Seventh Framework Program (FP-7-IDEAS-ERC), ERC Advanced grant (WAVETOMO).

#### References

- Archie, G. E. (1942), The electrical resistivity log as an aid in determining some reservoir characteristics, *Trans. AIME*, *146*, 54–62.
- Baird, A. F., J.-M. Kendall, and D. A. Angus (2013), Frequency-dependent seismic anisotropy due to fractures: Fluid flow versus scattering, *Geophysics*, *78*, WA111–WA122, doi:10.1190/geo2012-0288.1.
- Benveniste, Y. (1987), A new approach to the application of Mori-Tanaka theory in composite-materials, *Mech. Mater.*, *6*, 147–157.
- Berryman, J. (1997), Generalization of Eshelby's formula for a single ellipsoidal elastic inclusion to poroelasticity and thermoelasticity, *Phys. Rev. Lett.*, *79*, 1142–1145.
- Berryman, J. G., and S. Nakagawa (2010), Inverse problem in anisotropic poroelasticity: Drained constants from undrained ultrasonic measurements, *J. Acoust. Soc. Am.*, *127*, 720–729.
- Biot, M. A. (1955), Theory of elasticity and consolidation for a porous anisotropic solid, *J. Appl. Phys.*, *26*, 182–185.
- Biot, M. A. (1962), Mechanics of deformation and acoustic propagation in porous media, *J. Appl. Phys.*, *33*, 1482–1498.
- Biot, M. A., and D. G. Willis (1957), The elastic coefficients of the theory of consolidation, *J. Appl. Mech.*, *24*, 594–601.
- Castagna, J. P., M. L. Batzle, and R. L. Eastwood (1985), Relationships between compressional-wave and shear-wave velocities in clastic silicate rocks, *Geophysics*, *50*, 571–581.
- Chapman, M. (2003), Frequency-dependent anisotropy due to meso-scale fractures in the presence of equant porosity, *Geophys. Prospect.*, *51*, 369–379, doi:10.1046/j.1365-2478.2003.00384.x.
- Chichinina, T. I., I. R. Bolentseva, and G. Ronquillo-Jarillo (2009), Anisotropy of seismic attenuation in fractured media: Theory and ultrasonic experiment, *Transp. Porous Med.*, *79*, 1–14.
- Dvorkin, J., G. Mavko, and A. Nur (1995), Squirt flow in fully saturated rocks, *Geophysics*, *60*, 97–107.
- Eshelby, J. (1957), The determination of the elastic field of an ellipsoidal inclusion, and related problems, *Proc. R. Soc. Lond. A*, *241*, 376–396.
- Gassmann, F. (1951), Über die elastizität poröser medien, *Vierteljahrsschrift der Naturforschenden Gesellschaft in Zürich*, *96*, 1–23.
- Gurevich, B., and S. L. Lopatnikov (1995), Velocity and attenuation of elastic waves in finely layered porous rocks, *Geophys. J. Int.*, *121*, 933–947.
- Johnson, D. L. (2001), Theory of frequency dependent acoustics in patchy-saturated porous media, *J. Acoust. Soc. Am.*, *110*, 682–694.
- Knight, R., J. Dvorkin, and A. Nur (1998), Acoustic signatures of partial saturation, *Geophysics*, *63*, 132–138.
- Landau, L. D., and E. M. Lifshitz (1980), *Statistical Physics*, 3rd ed., Pergamon, New York.
- Maewal, A., and D. P. Dandekar (1987), Effective thermoelastic properties of short-fiber composites, *Acta Mech.*, *66*, 191–204.
- Masson, Y. J., and S. R. Pride (2007), Poroelastic finite difference modeling of seismic attenuation and dispersion due to mesoscopic-scale heterogeneity, *J. Geophys. Res.*, *112*, B03204, doi:10.1029/2006JB004592.
- Masson, Y. J., and S. R. Pride (2014), A fast algorithm for invasion percolation, *Transp. Porous Media*, *102*, 301–312.
- Masson, Y. J., S. R. Pride, and K. T. Nihei (2006), Finite difference modeling of Biot's poroelastic equations at seismic frequencies, *J. Geophys. Res.*, *111*, B10305, doi:10.1029/2006JB004366.
- Maultzsch, S., M. Chapman, E. Liu, and X. Y. Li (2003), Modelling frequency-dependent seismic anisotropy in fluid-saturated rock with aligned fractures: Implication of fracture size estimation from anisotropic measurements, *Geophys. Prosp.*, *51*, 381–392.
- Mavko, G., and A. Nur (1979), Wave attenuation in partially saturated rocks, *Geophysics*, *44*, 161–178.
- Mori, T., and K. Tanaka (1973), Average stress in matrix and average elastic energy of materials with misfitting inclusions, *Acta Metal.*, *21*, 571–574.
- Mura, T. (1982), *Micromechanics of Defects in Solids*, Martinus Nijhoff Publishers, The Hague, Netherlands.
- Murphy, W. F., III (1982a), Effects of partial water saturation on attenuation in Massillon sandstone and Vycor porous-glass, *J. Acoust. Soc. Am.*, *71*, 1458–1468.
- Murphy, W. F., III (1982b), Effects of microstructure and pore fluids on the acoustic properties of granular sedimentary materials, PhD thesis, Stanford Univ., Stanford, Calif.
- Norris, A. N. (1993), Low-frequency dispersion and attenuation in partially saturated rocks, *J. Acoust. Soc. Am.*, *94*, 359–370.
- O'Connell, R. J., and B. Budiansky (1978), Measures of dissipation in viscoelastic media, *Geophys. Res. Lett.*, *5*, 5–8.
- Pan, H., and G. Weng (1995), Elastic-moduli of heterogeneous solids with ellipsoidal inclusions and elliptical cracks, *Acta Mech.*, *110*, 73–94.

- Pride, S. R. (2005), Relationships between seismic and hydrological properties, in *Hydrogeophysics*, edited by Y. Rubin and S. Hubbard, pp. 253–291, Springer, The Neth.
- Pride, S. R., and J. G. Berryman (2003a), Linear dynamics of double-porosity and dual-permeability materials. I. Governing equations and acoustic attenuation, *Phys. Rev. E*, *68*, 036,603, doi:10.1103/PhysRevE.68.036604.
- Pride, S. R., and J. G. Berryman (2003b), Linear dynamics of double-porosity and dual-permeability materials. II. Fluid transport equations, *Phys. Rev. E*, *68*, 036,604.
- Pride, S. R., J. G. Berryman, and J. M. Harris (2004), Seismic attenuation due to wave-induced flow, *J. Geophys. Res.*, *109*, B01201, doi:10.1029/2003JB002639.
- Skempton, A. W. (1954), The pore-pressure coefficients A and B, *Geotechnique*, *4*, 143–147.
- Toksöz, M. N., D. H. Johnston, and A. Timur (1979), Attenuation of seismic waves in dry and saturated rocks: I. Laboratory measurements, *Geophysics*, *44*, 681–690.
- Walpole, L. J. (1981), Elastic behavior in composite materials: Theoretical foundations, in *Advances in Applied Mechanics*, vol. 21, edited by C.-S. Yih, pp. 169–236, Acad. Press, New York.
- White, J. E. (1975), Computed seismic speeds and attenuation in rocks with partial gas saturation, *Geophysics*, *40*, 224–232.
- White, J. E., N. G. Mikhaylova, and F. M. Lyakhovitsky (1975), Low-frequency seismic waves in fluid-saturated layered rocks, *Izvestija Academy of Sciences USSR, Phys. Solid Earth*, *11*, 654–659.
- Wilkinson, D., and J. F. Willemsen (1983), Invasion percolation: A new form of percolation theory, *J. Phys. A: Math. Gen.*, *16*, 3365, doi:10.1088/0305-4470/16/14/028.
- Wong, R. C. K., D. R. Schmitt, D. Collis, and R. Gautman (2008), Inherent transversely isotropic elastic parameters of over-consolidated shale measured by ultrasonic waves and their comparison with static and acoustic in situ log measurements, *J. Geophys. Eng.*, *5*, 103–117.